The Electrochemical Society
Advancing solid state & electrochemical science & technology

Alkali Metal Salt Interference on the Salicylate Method for Quantifying Ammonia from Nitrogen Reduction

View the article online for updates and enhancements.

Alkali Metal Salt Interference on the Salicylate Method for Quantifying Ammonia from Nitrogen Reduction

Juan José Giner-Sanz,[1,2,z] **Graham M. Leverick,**[3] **Livia Giordano,**[1,4] **Valentín Pérez-Herranz,**[2] and **Yang Shao-Horn**[1,3,5,*,z]

[1]*Research Laboratory of Electronics, Massachusetts Institute of Technology, Cambridge, Massachusetts 02139, United States of America*
[2]*IEC group, Depto. Ingeniería Química y Nuclear, Universitat Politècnica de València, Camí de Vera s/n, Valencia 46022, Spain*
[3]*Department of Mechanical Engineering, Massachusetts Institute of Technology, Cambridge, Massachusetts 02139, United States of America*
[4]*Dipartimento di Scienza dei Materiali, Università di Milano-Bicocca, Milano 20136, Italy*
[5]*Department of Materials Science and Engineering, Massachusetts Institute of Technology, Cambridge, Massachusetts 02139, United States of America*

The salicylate method has been extensively used for quantifying ammonia in the emerging field of nitrogen (electro)fixation. Alkali metal salts are widely used as supporting electrolytes for nitrogen reduction, especially in the context of electrochemical nitrogen fixation. However, these salts are known to cause interferences on the salicylate method, introducing significant uncertainties in ammonia quantification. In this work, the interference of lithium, sodium and potassium chlorides, perchlorates and sulfates on the ammonia quantification results obtained using the salicylate method was experimentally quantified, and an empirical model was developed to capture the effect of the presence of these interferents on the ammonia quantification by the salicylate method. Based on the obtained experimental interference results, the tested interferents can be ranked from stronger interferent (i.e. lower admissible concentration) to weaker interferent: Li_2SO_4, $KClO_4$, $LiCl$, $LiClO_4$, K_2SO_4, $NaClO_4$, $NaCl$, Na_2SO_4, KCl. The developed model can be used to assess the experimental error in ammonia quantification from nitrogen reduction, in samples containing these interferents. This model can be used to correct the interferences on the ammonia quantification, when the interferent concentration in a sample is known (or measurable).

List of Symbols

Roman symbols

A_λ	Absorbance at wavelength λ
C	Molar concentration ($mol \cdot m^{-3}$)
CL	Confidence level
e	Relative error
l	Optical path (m)
R^2	Determination coefficient

Greek symbols

α_Γ	Absorbance sensibility coefficient ($mol^{-1} \cdot m^3$)
α_Γ^i	Ion i individual absorbance sensibility coefficient ($mol^{-1} \cdot m^3$)
α_λ	Peak displacement slope ($m \cdot mol^{-1} \cdot m^3$)
α_λ^i	Ion i individual peak displacement slope ($m \cdot mol^{-1} \cdot m^3$)
$\Delta\Gamma$	Maximum change in the interference coefficient
$\Delta\Gamma^i$	Ion i individual maximum change in the interference coefficient
$\varepsilon^\star$	Effective molar attenuation coefficient ($m^3 \cdot mol^{-1} \cdot m^{-1}$)
Γ	Interference coefficient
λ	Wavelength (m)
λ_{max}	Wavelength of the peak maximum (m)

Subscripts

TAN	Total ammonia nitrogen (i.e. $NH_3 + NH_4^+$)

Superscripts

Sample	In the initial sample (i.e. before the reagent additions)

*Electrochemical Society Member.
[z]E-mail: juagisan@etsii.upv.es; shaohorn@mit.edu

Nitrogen is one of the main chemical elements required for life.[1] Although the Earth's atmosphere is mainly made of nitrogen, most of it is not directly available to living organisms.[1] The combination of thermodynamic stability[2] and kinetic hindrance[3] makes the process of N_2 fixation into biologically available nitrogen forms a very non-favorable process, making biologically available nitrogen compounds (such as ammonia and urea) precious resources for human societies. The state-of-the-art artificial N_2 fixation method is the Haber-Bosch process for ammonia synthesis.[4] This process was developed by Fritz Haber in order to lower the dependence of Germany on Chilean nitrate and Peruvian guano, the natural fertilizers used prior to the industrial production of ammonia; and was subsequently scaled up by Carl Bosch. Since then, the Haber-Bosch process has become one of the major backbones that has enabled the 20th century boom in human population.[5] Currently, more than 170 million metric tons of ammonia are produced each year,[6] more than 90% of which are synthetized using the Haber-Bosch process.[7] Around 80% of this ammonia is used as synthetic fertilizer,[8,9] sustaining in this way nearly two-fifths of the World's population.[10] In addition to its importance in food production, ammonia is also a key compound for the chemical industry,[11] where every nitrogen atom in synthetic molecules comes from it.[12] Moreover, currently[13] ammonia is viewed as a potential renewable energy carrier,[14] and hydrogen carrier.[15]

The current Haber-Bosch process works at 400–450 °C and 150–250 bar, and uses iron or ruthenium-based catalysts.[16] These harsh operation conditions make the Haber-Bosch process a very energy-intensive process[17] (i.e. it consumes between 1% and 2% of the anthropogenic energy[18–20]); and make the distributed ammonia production economically unfeasible,[21] restricting ammonia production to large centralized ammonia production facilities.[22] In addition to its large energy consumption, the current Haber-Bosch process is an

important CO_2 source (i.e. responsible for nearly 1.44% of the total CO_2 emissions[23]) due to its reliance on fossil fuels[24] (mainly natural gas) as hydrogen source.[25] In recent years, momentum has been building in the scientific community to develop an ammonia production process that operates at milder conditions (ideally at ambient conditions) based on renewable sources of hydrogen and energy.[26] Achieving this goal would make ammonia production more sustainable and economically profitable, enabling smaller local reactors,[27] and thereby distributed ammonia production networks in which ammonia would be directly generated at the consumption point. To present date, several promising strategies are being actively explored, including (mild conditions) thermochemical,[28–30] electrochemical,[31–34] photochemical,[35–37] photoelectrochemical,[38–40] plasma-activated,[41,42] and mechanocatalytical[21,43] ammonia production methods. So far, none of these methods has achieved acceptable ammonia yields and/or selectivities, and therefore the search continues as shown by the increasing number of works dealing with the Nitrogen Reduction Reaction (NRR). The main parameters that are measured in every NRR experiment are the ammonia yield and some parameter related to selectivity (v.g. in electrochemical NRR experiments, the faradic efficiency). In order to obtain these parameters, the produced ammonia must be quantified,[44] and therefore accurate, sensitive and reproducible ammonia quantification methods are required. Several ammonia quantification methods are available nowadays,[45,46] the most widely used ones are spectrophotometric (i.e. colorimetric) methods,[47,48] ammonia ion-selective based methods,[49] biosensors,[50] ion chromatography,[51,52] Fourier Transform Infrared Radiation (FTIR) spectroscopy,[53] and ^{1}H NMR spectroscopy.[54] A large number of the works of the NRR field are not reproducible due to the use of non-rigorous protocols prone to interferences from adventitious contamination with ammonia from non-NRR sources.[55] In order to solve these reproducibility problems, rigorous protocols for NRR experiments have been proposed in recent years.[44,55,56] All these protocols involve ^{15}N isotopic labelling for distinguishing unequivocally the ammonia generated by NRR from the contamination due to non-NRR related sources of ammonia. The main issue of ^{15}N isotopic labelling is its prohibitively high cost, even when the amount of [15]N_2 is reduced by using a closed system.[27] For this reason, colorimetric methods are still widely used for initial screening experiments, which can be then validated using ^{15}N isotopic labelling.

The salicylate method is one of the colorimetric methods available today for quantifying ammonia, which is based on the addition of sodium salicylate, sodium hypochlorite and sodium nitroprusside (that acts as a catalyst) to a sample containing ammonia. After the reagent addition, the mixture undergoes a Berthelot reaction that produces an indophenol-type dye that strongly absorbs visible light between 630 nm and 720 nm, allowing to quantify ammonia using ultraviolet–visible spectroscopy.[57] The major advantage of the salicylate method over the other available colorimetric methods is that it neither requires toxic reagents (such as phenol in the Indophenol method, and mercury salts in the Nessler Method),[58,59] nor generates toxic fumes (such as ortho-chlorophenol produced by the Indophenol method).[60] The main limitation of the Berthelot methods (that include the salicylate method) is that they are prone to a number of interferences,[61] such as pH,[62] nitrogen-containing compounds,[63] and metal ions,[64] amongst many others, which can lead to errors in the ammonia quantification if not properly accounted for. Alkali metal salts such as lithium salts, are known to be one of these interferents for the Berthelot methods.[65] Such salts are used extensively as supporting electrolytes for NRR experiments, especially in electrochemical nitrogen fixation experiments, where lithium,[31] sodium[66,67] and potassium[32,68–70] chlorides,[70,71] perchlorates[31] and sulfates[32,66–68] can be found ubiquitously. Despite their widespread use, to the best of our knowledge, no previous work has quantitatively studied the interferences of these alkali metal salts on the ammonia quantification results obtained with the salicylate method.

In this work, the interference of lithium, sodium and potassium chlorides, perchlorates and sulfates on the ammonia quantification results obtained using the salicylate method was experimentally quantified, and an empirical model was developed to model the effect of the presence of these interferents on the ammonia quantification by the salicylate method. The developed model can be used to assess and correct the experimental errors in ammonia quantification during NRR experiments when the salicylate method is used for quantifying ammonia in samples that contain alkali metal salts (i.e. Period 2, 3 and 4 alkali metal chlorides, perchlorates and sulfates).

Experimental Methods

Materials.—Ammonium chloride (Sigma-Aldrich, ACS reagent ⩾99.5%), lithium chloride (Alfa Aesar, anhydrous 99%), lithium perchlorate (Sigma-Aldrich, ACS reagent), lithium sulfate mono-hydrate (Sigma-Aldrich, ACS reagent ⩾99.0% dry basis), sodium chloride (Sigma-Aldrich, ACS reagent ⩾99.0%), sodium perchlorate (Sigma-Aldrich, ACS reagent ⩾98.0%), sodium sulfate (Sigma-Aldrich, ACS reagent ⩾99.0%, anhydrous powder), potassium chloride (Alfa Aesar, 99%), potassium perchlorate (Sigma-Aldrich, ACS reagent ⩾99%), potassium sulfate (Sigma-Aldrich, ACS reagent ⩾99.0%, powder), sodium salicylate (Ensure Millipore, for analysis), sodium nitroprusside dihydrate (Ensure Millipore, for analysis), sodium citrate dihydrate (Ensure Millipore, for analysis), sodium hydroxide (Sigma-Aldrich, ACS reagent, anhydrous free-flowing pellets) and the sodium hypochlorite aqueous solution (Sigma-Aldrich, reagent grade, available chlorine 4.00%–4.99%) were all used as received. All the reagents were stored at room temperature, except the sodium hypochlorite aqueous solution, which was stored at 5 °C. Deionized (DI) water was obtained from a Millipore system (Resistivity: 18.2 MΩ·cm at 25 °C; TOC: 4 ppb), and was always freshly prepared just before its use. The samples were stored and manipulated in scintillation vials (SciLabware, 20 ml). 3 ml disposable methacrylate cuvettes (VWR, 1 cm optical path) were used for UV–Visible measurements. A GENESYS® 180 UV–Visible spectrophotometer was used to measure the UV–Visible spectra.

The salicylate method.—From all the variants of the salicylate method available today in literature, a modified version of the Bower-Holm-Le-Boyd method,[72,73] optimized in previous work,[74] was used here. The salicylate catalyst solution (Solution R1) was prepared by dissolving sodium salicylate powder and sodium nitroprusside dihydrate flakes in freshly prepared DI water in order to obtain a 2.75 M sodium salicylate and 0.95 mM sodium nitroprusside solution. The alkaline citrate solution (Solution R2) was prepared by dissolving sodium citrate dihydrate powder and sodium hydroxide pellets in order to obtain a 340 mM sodium citrate and 465 mM sodium hydroxide solution. Finally, the alkaline hypo-chlorite solution (Solution R3) was obtained by mixing 10 vol% of commercial 5% sodium hypochlorite aqueous solution with solution R2. Solutions R1 and R3 were always freshly prepared prior to the sample analysis, and were not stored afterwards. On the contrary, solution R2 was prepared in advanced, and stored at room temperature. Furthermore, solution R1 was kept in an opaque dark bottle during the whole analysis process.

The procedure to analyze a given sample encompasses two successive reagent additions and a color development period. The first addition step consisted of mixing 5 ml of the sample to analyze with 600 μl of solution R1, and shaking the mixture vigorously. The second addition step consisted of mixing the mixture obtained in the previous step with 1 ml of solution R3, and shaking the mixture vigorously. This step was performed in the dark, and after it, the sample was stored in the dark for 1 h. Following this color development period, the visible spectra of the mixture was measured using a double beam spectrophotometer. Since the salicylate reagents (especially sodium nitroprusside) have color (Fig. S1 (available online at stacks.iop.org/ECSA/1/024501/mmedia)), a blank sample was prepared by applying the above procedure to

5 ml of freshly prepared DI water. This blank sample was used as blank and reference sample (i.e. double beam spectrophotometer) during the UV–Visible measurement of the different samples. Both, the sample preparation and the spectrum measurement, were done at ambient temperature. All the visible spectra were measured from 850 nm to 350 nm, with a step size of 0.5 nm and a sweep speed of 5 nm·s^{-1}.

Absorbance-vs-ammonia concentration calibration curves.—An ammonium parent solution of 0.8 mM Total Ammonia Nitrogen (TAN, i.e. NH$_3$ + NH$_4^+$), was prepared by dissolving solid NH$_4$Cl powder in freshly prepared DI water. A set of solutions of different TAN concentrations (in the linearity region) were prepared by successive dilutions of the parent solution. In the case of the interferent-free calibration curve, freshly prepared DI water was used for preparing the parent solution and its daughter dilutions; whereas in the case of the calibration curve in the presence of a given interferent (i.e. lithium, sodium or potassium chloride, perchlorate or sulfate), an interferent solution of the corresponding concentration was used for this matter. The interferent solution was prepared by dissolving the required amount of the interferent solid (i.e. lithium, sodium or potassium chloride, perchlorate or sulfate) in freshly prepared DI water. The different sets of calibration samples were analyzed using the salicylate method protocol described above.

Interference measurements.—A 1.5 mM TAN ammonium parent solution was prepared by dissolving solid NH$_4$Cl in freshly prepared DI water. Interference measurements were carried out for nine interferents: lithium chloride, perchlorate and sulfate; sodium chloride, perchlorate and sulfate; and potassium chloride, perchlorate and sulfate. A set of samples was prepared for each one of these interferents. Each set of samples was formed by 5 ml samples of different interferent concentrations and a given TAN concentration, prepared by dissolving the required amounts of the solid interferent in the ammonium parent solution, and then diluting accordingly using freshly prepared DI water. Following this procedure, all the prepared samples had the same ammonia concentration; and what changed from sample to sample was the interferent (from one set to another), and the interferent concentration (within a given set of samples).

The different sets of samples were analyzed using the salicylate method protocol described in above. The order in which the reagents were added to the samples within a given set of samples (and therefore, the order in which the UV–Visible spectra were measured) was random (i.e. neither in increasing or decreasing interferent concentration order); except for the blank sample, which was left at the end of the addition queue. This randomization strategy was used in order to orthogonalize the interferent concentration factor from the order factor, ensuring in this way that any trend observed is actually due to the interferent concentration effect.[64]

DFT calculations.—The UV–Visible spectra were simulated by computing the electronic excitations of the dye and dye-cations complexes in water, where the solvent was simulated with an implicit solvation model (PCM).[75] The ground state structures were obtained by Density Functional Theory (DFT) with a standard force-minimization process with a 6–311 G(d,p) basis set, and the vibrational spectrum was determined to verify that all vibrational frequencies were real. Time-dependent DFT (TD-DFT) was used to compute the ten first low-lying excited states of each system, where the solvent was treated with the so-called nonequilibrium procedure, specifically designed for the study of absorption processes.[76,77] The PBE0 functional[78,79] and the 6–311 + G(d,p) basis set were used for the TD-DFT calculations. All calculations were performed with the Gaussian (g16) suite.[80]

Results and Discussion

Absorbance-vs-ammonia concentration calibration.—Similar spectrum features were observed in UV–Visible spectra when the salicylate method was applied to samples with Total Ammonia Nitrogen (TAN, i.e. NH$_3$ + NH$_4^+$) concentrations from 0.00 to 0.15 mM both with (Fig. 1b) and without (Fig. 1a) 0.5 M LiClO$_4$. The most remarkable feature of these spectra is the indophenol peak that appears around 650 nm, which can be attributed to the indophenol-type dye formed due to the reaction between ammonia in the sample and the salicylate method reagents (sodium salicylate and sodium hypochlorite, Fig. S2).[74] While the presence of LiClO$_4$ in the sample does not generate any new spectrum features in the final spectrum, it causes a hypsochromic shift (i.e. blue shift) and a
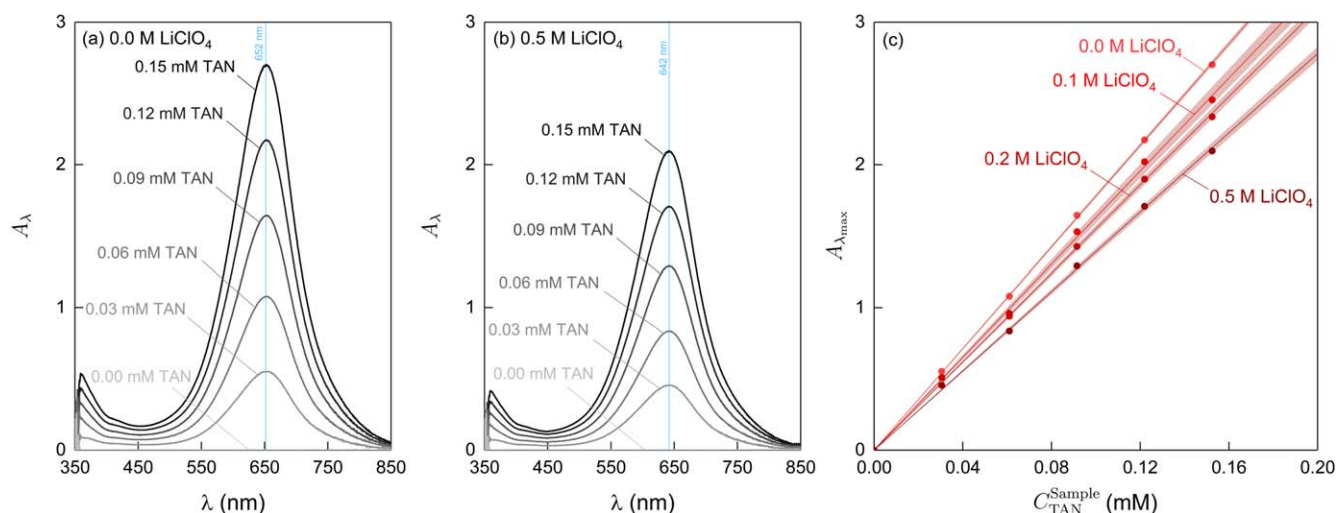

Figure 1. UV–Visible spectra (i.e. absorbance, A_λ; as a function of wavelength, λ) obtained using the salicylate method on (a) the water calibration samples (i.e. different TAN concentrations in water) and on (b) the 0.5 M LiClO$_4$ calibration samples (i.e. different TAN concentrations in 0.5 M LiClO$_4$ solution). In all cases, the spectra were measured against the reference sample, from 850 nm to 350 nm with a step size of 0.5 nm and a sweep speed of 5 nm·s^{-1}. (c) The calibration curves obtained by representing the peak maximum absorbance ($A_{\lambda_{max}}$) as a function of the TAN concentration in the sample (C_{TAN}^{Sample}), for different LiClO$_4$ concentrations in the sample (spectra in Fig. S3). The dots correspond with the experimental points, the lines are the fitted linear regression lines, and the coloured regions are the regression 95% confidence bands. From the slopes of the fitted lines, and the optic path of the used cuvettes ($l = 1 cm$), the effective molar attenuation coefficient were determined: for the water calibration, $\varepsilon* = 17.80 \pm 0.12(95\% CL)$mM^{-1}·cm^{-1} ($R^2 = 99.99\%$); for the 0.1 M LiClO$_4$ calibration, $\varepsilon* = 16.30 \pm 0.41(95\% CL)$mM^{-1}·cm^{-1} ($R^2 = 99.94\%$); for the 0.2 M LiClO$_4$ calibration, $\varepsilon* = 15.49 \pm 0.25(95\% CL)$mM^{-1}·cm^{-1} ($R^2 = 99.97\%$); and for the 0.5 M LiClO$_4$ calibration, $\varepsilon* = 13.90 \pm 0.24(95\% CL)$mM^{-1}·cm^{-1} ($R^2 = 99.97\%$).

hypochromic shift (i.e. decrease in absorbance) of the indophenol peak (Figs. 1a, 1b and S2). For instance, the addition of 0.5 M LiClO$_4$ shifts the peak maximum from 652 nm (without LiClO$_4$) to 642 nm while the peak maximum absorbance decreases from around 2.5 to 2.0. Therefore, LiClO$_4$ can be considered as an interferent of the salicylate method that results in a combined hypsochromic-hypochromic shift in the spectrum.

The absorbance with TAN concentration at different amounts of LiClO$_4$ retained linear relationships, where decreasing effective molar attenuation coefficient of the indophenol dye was found with increasing LiClO$_4$ concentration. To accommodate the hypsochromic interference of LiClO$_4$, calibration curves of TAN for each LiClO$_4$ concentration were obtained using the maximum peak absorbance, as opposed to the absorbance at a given wavelength, as a function of the TAN concentration in the sample (Fig. 1c). Significantly, the calibration curves were found linear for different LiClO$_4$ concentrations, with determination coefficients (R^2) above 99.9%; including 99.99% for 0.0 M LiClO$_4$, 99.94% for 0.1 M LiClO$_4$, 99.97% for 0.2 M LiClO$_4$, and 99.97% for 0.5 M LiClO$_4$. While the presence of LiClO$_4$ does not break the linearity of the calibration curve, the hypochromic shift of the indophenol peak it produces, considerably reduces the effective molar attenuation coefficient of the indophenol dye, from 17.8 to 13.9 mM^{-1}·cm^{-1} in 0.5 M LiClO$_4$. Therefore, using the water calibration curve for quantifying ammonia in samples containing 0.5 M LiClO$_4$ would result in an error in the ammonia concentration of 28%. These results show the significant effect that interferences can have on the ammonia quantification results; which calls for the need of correcting the interferences on the salicylate method.

Interference experiments for different interferents.—In this work, nine interference experiments were performed (Fig. 2), for nine interferents including LiCl, LiClO$_4$, Li$_2$SO$_4$, NaCl, NaClO$_4$, Na$_2$SO$_4$, KCl, KClO$_4$, and K$_2$SO$_4$. All of the interferents considered in this work were found to cause a hypsochromic shift (i.e. blue shift) in the dye spectrum. Interestingly, while the three Li-containing interferents caused a strong hypochromic shift in the dye spectrum (i.e. a decrease in absorbance), all of the other considered interferents caused a slight to moderate hyperchromic shift in the dye spectrum (i.e. increasing in absorbance). Moreover, by comparing the UV–visible spectra of samples where the interferents were present in the original samples to those where the interferents were introduced following the dye formation reaction (Fig. S4), we found that Li-containing interferents might cause interference by a different mechanism than Na- and K- containing interferents. For instance, for the lithium salts (LiCl, LiClO$_4$ and Li$_2$SO$_4$), the spectra obtained when the interferent was added before the dye production and when it was added after the dye production differed significantly from the one obtained when no lithium salt was added (Fig. S4). On the other hand, for sodium and potassium salts (NaCl, NaClO$_4$, Na$_2$SO$_4$, KCl, KClO$_4$ and K$_2$SO$_4$), only the spectrum obtained when the interferent was added before dye production differed from the spectrum without interferent, whereas adding the interferent after the dye was formed, produced no discernable difference. Such findings suggest that Na- and K-containing interferents can alter the dye formation reaction, whereas Li-containing interferents may alter the dye formation reaction but also alter the intrinsic absorbance of the indophenol dye after it is formed.

Time-dependent density functional theory (TD-DFT) calculations suggest that hypsochromic shift in the indophenol dye peak absorbance wavelength stems from coordination between the dye and cations in the solution, whereas hypochromic and hyperchromic shifts in the dye's molar absorbance stem from differing populations of the *cis-* and *trans-* isomers of the dye. In order to gain further mechanistic insights into the physical origin of the interferences observed in this study, TD-DFT calculations were performed on the uncoordinated indophenol dye in an implicit aqueous solvation environment, as well as with Li$^+$, Na$^+$ and K$^+$ coordination at a PBE0 level of theory to generate simulated UV–Visible spectra (Fig. S8, Table S2). TD-DFT computed UV–visible spectra of the indophenol dye showed a peak absorbance of 540 nm, which is blue-shifted by $\sim$110 nm from the experimental peak absorbance of 652 nm. This shift is considered reasonable for TD-DFT calculations of UV–Visible spectra.[81] Notably, both *cis-* and *trans-* isomers of the uncoordinated indophenol dye had similar formation energies and peak absorbance wavelengths (Table S2), but the *cis-* isomer had lower simulated molar absorbance (Fig. S8a). Upon the introduction of cation coordination, the peak absorbance wavelength was blue shifted from 540 nm for no cation coordination, to 530 nm with K$^+$, 527 nm with Na$^+$ and 526 nm with Li$^+$ coordination, where similar blue shifts were observed for both the *cis-* and *trans-* isomers (Fig. S8). Therefore, we attribute the hypsochromic shift from the nine interferents considered in this study to primarily stem from cation coordination with the indophenol dye. In addition we hypothesize that the hypochromic and hyperchromic shifts from the considered interferents stem from different populations of the *cis-* and *trans-* isomers of the indophenol dye, where large cations like Na$^+$ and K$^+$ might sterically hinder the formation of the *cis-* isomer during the dye formation reaction, leading to higher selectivity for the *trans-* isomer and thus higher molar absorbance. This hypothesis is supported by the finding that cation coordination subtly shifted the relative formation energies of the *cis-* and *trans-* isomers, making the *cis-* isomer slightly more favorable (Table S2). We further postulate that Li$^+$ coordination may not lead to a kinetic preference for the *cis-* isomer during dye formation, but may further cause isomerization of the formed dye. While the stereochemistry of the indophenol dye offers a possible explanation for the observed hypochromic and hyperchromic shifts of the considered interferents, further work is needed to fully support this hypothesis.

Interestingly, there is a moderate nonlinear correlation between the peak displacement and the experimental quantification error (Fig. S5). Consequently, the peak position (i.e. its displacement with respect to 652 nm) can be used as a weak indicator of the existence (and magnitude) of the interferences (of the interferents considered in this work) on the indophenol peak. Although this indicator can be used as a warning sign, unfortunately, the correlation is not strong enough in order to use the peak position as a corrector of the interference effect.

Modelling the interference on the salicylate method.—The interference on the salicylate method caused by the interferents considered in this work can be well-describe by a no-background multiplicative interference model. The interference is only a function of the interferent concentration, and does not depend on the TAN concentration. Unlike other interferents such as Fe III,[64] the presence of the interferents considered in this work does not generate a nonzero background absorbance, as shown by the absence of vertical translations of the calibration curves (i.e. all the calibration curves in Fig. 1c go through the origin). Therefore, we model the interference of the considered interferents on the salicylate method as follows:

$$A_{\lambda_{\max}(C_{Int}^{Sample})}(C_{TAN}^{Sample}; C_{Int}^{Sample})$$

$$= l \cdot \varepsilon_{\lambda_{\max}(C_{Int}^{Sample}=0)}^{\star}(C_{Int}^{Sample}=0) \cdot \Gamma(C_{Int}^{Sample}) \cdot C_{TAN}^{Sample} \quad [1]$$

Where C_{TAN}^{Sample} and C_{Int}^{Sample} are the concentration of TAN and interferent in the sample, respectively; $A_{\lambda_{max}}$ is the peak absorbance; l is the light optic path; and $\varepsilon_{\lambda_{\max}(C_{Int}^{Sample}=0)}^{\star}(C_{Int}^{Sample}=0)$ is the effective molar attenuation coefficient when no interferent is present (related to the slope of the calibration curve in water samples). Γ represents the interference coefficient, which captures the effect of the interferent on the effective molar attenuation coefficient of the
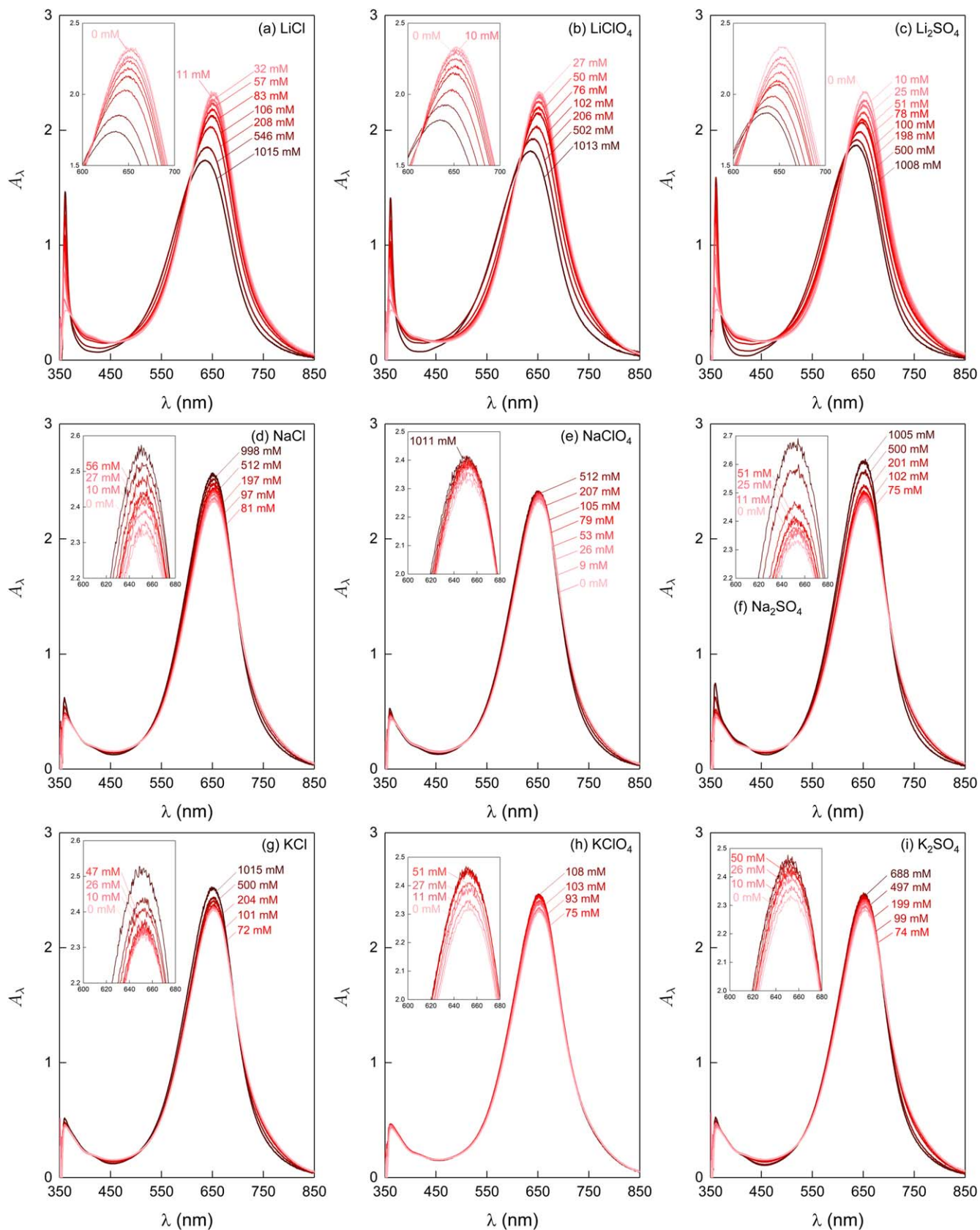
Figure 2. Effect of the interferent concentration in the sample on the UV–Visible spectra obtained by the salicylate method, for a given TAN concentration, for different interferents: (a) LiCl, (b) LiClO$_4$, (c) Li$_2$SO$_4$, (d) NaCl, (e) NaClO$_4$, (f) Na$_2$SO$_4$, (g) KCl, (h) KClO$_4$, (i) K$_2$SO$_4$. UV–Visible spectra (i.e. absorbance, A_λ; as a function of wavelength, λ) obtained using the salicylate method on samples with different interferent concentrations, and a given TAN concentration (C_{TAN}^{Sample} = 0.12mM). In all cases, the spectra were measured against the reference sample, from 850 nm to 350 nm with a step size of 0.5 nm and a sweep speed of 5 nm·s^{-1}. Insets: zoom of the peak region.

dye. The main assumption of this multiplicative interference model is that the aforementioned interference coefficient only depends on the interferent concentration, and does not depend on the ammonia concentration. The interference coefficient for a given interferent concentration is defined as the ratio between the maximum absorbance with and without the considered interferent concentration:

$$\Gamma(C_{Int}^{Sample}) \equiv \frac{A_{\lambda_{\max}(C_{Int}^{Sample})}(C_{TAN}^{Sample};\ C_{Int}^{Sample})}{A_{\lambda_{\max}(C_{Int}^{Sample}=0)}(C_{TAN}^{Sample};\ C_{Int}^{Sample}=0)} \qquad [2]$$

Based on this definition, the interference coefficient is a dimensionless coefficient that quantifies the magnitude of the interference, where $\Gamma = 1$ corresponds to the case of no interference. The absolute deviation of Γ from one (i.e. $|\Gamma - 1|$) quantifies the magnitude of the interference: $\Gamma > 1$ corresponds to hyperchromic interferences (i.e. positive interferences); while $\Gamma < 1$ corresponds to hypochromic interferences (i.e. negative interferences). To compute the interference coefficients, the experimental spectra in Fig. 2 were fitted to Gaussian peaks:

$$A_\lambda = A_{\lambda_{max}} \cdot \exp\left[\left(-\frac{2\sqrt{\ln(2)} \cdot (\lambda - \lambda_{\max})}{\text{FWHM}}\right)^2\right] \qquad [3]$$

which includes three fitting parameters: the peak position ($\lambda_{\max}$), the peak maximum absorbance ($A_{\lambda_{max}}$), and the Full Width at Half Maximum (FWHM) that quantifies the width of the peak. From the fitting of the different spectra, the peak position was obtained (black points in Fig. 3), and the interference coefficient was calculated using Eq. 2 (blue points in Fig. 3), for each interferent and interferent concentration.

Interference models.—The peak position was found to decrease linearly with the interferent concentration for all the interferents considered in this work (Fig. 3). Based on this observation, a linear empirical model was proposed to capture the effect of the interferent concentration on the peak position (peak displacement model):

$$\lambda_{\max}(C_{Int}^{Sample}) = \lambda_{\max}(C_{Int}^{Sample} = 0) - \alpha_\lambda \cdot C_{Int}^{Sample} \qquad [4]$$

Where $\lambda_{\max}(C_{Int}^{Sample} = 0)$ is the peak position in the absence of interferent (i.e. 652 nm), and α_λ denotes the peak displacement slope, that corresponds to the peak (blue) shift produced by a unitary change in the interferent concentration. The interference coefficient was shown to follow an asymptotically exponential relation with the interferent concentration for both the hypochromic and the hyperchromic interferents considered in this work (Fig. 3). For low interferent concentrations, the interference coefficient changes linearly with the interferent concentration. The linear trend progressively flattens for higher interferent concentrations until it reaches an asymptotic limit, after which further increases in the interferent concentration do not cause further changes in the interference coefficient. Based on this observation, an exponential empirical model was proposed to capture the effect of the interferent concentration on the interference coefficient (interference model):

$$\Gamma(C_{Int}^{Sample}) = 1 + \Delta\Gamma \cdot (1 - e^{-\alpha_\Gamma \cdot C_{Int}^{Sample}}) \qquad [5]$$

The proposed interference model has two parameters: $\Delta\Gamma$ which gives is the maximum change (for very large interferent concentrations) in the interference coefficient and α_Γ (the absorbance sensibility coefficient) which quantifies the sensibility of the interference coefficient to the interferent concentration. Encouragingly, the asymptotic behavior of the interference coefficient is consistent with the interference mechanisms proposed above. For instance, there is a maximum number of ions that can interact with the dye,

where further interferent concentration increases do not lead to higher coordination with the dye when the corresponding interferent concentration is reached, resulting in the asymptotic behavior observed for high interferent concentrations.

The proposed peak displacement and interference models (Fig. 4 and Table I) allow for an accurate description of the influence of the nine interferents considered in this work. Fitting the experimental data points from Fig. 3 to Eqs. 4 and 5 results in high determination coefficients of the fitted models (Table I) as well as good visual agreement between the predictions of the models and the experimental data (Fig. 3). We note of the different model parameters (α_λ, $\Delta\Gamma$ and α_Γ), that the maximum change in the interference coefficient ($\Delta\Gamma$) and the peak displacement slope (α_λ) are moderately correlated, whereas the other two pairs of parameters present no correlation (Fig. S6). In the (α_λ; $\Delta\Gamma$) plane, two well defined clusters can be identified (Fig. S6a): one associated with the Li salts, with high peak displacement slopes (i.e. large peak displacement for an unitary change in the interferent concentration) and negative maximum changes in the interference coefficient (i.e. negative interference on the indophenol peak); and another associated with the Na and K salts, with low peak displacement slopes (i.e. small peak displacement for an unitary change in the interferent concentration) and positive maximum changes in the interference coefficient (i.e. positive interference on the indophenol peak). The existence of these two distinct clusters is consistent with the fact that Li-containing interferents were able to alter the absorbance properties of the indophenol dye even after its formation, whereas Na- and K-interferents only altered the dye formation reaction.

The maximum relative errors in ammonia quantification due to the presence of lithium, sodium or potassium chlorides, perchlorates or sulfates in the sample, range from 5 to 25%. The fitted interference models were used to estimate the relative error in the ammonia quantification using the salicylate method due to the presence of different interferents in the sample (Fig. 5b), where this relative error is independent of the TAN concentration in the sample. As shown in Figs. 5a and 5b, the errors from Li-containing interferents were larger (peak shift $\leqslant$20 nm and relative error $\leqslant$25%) than those of Na- and K-interferents (peak shift $\leqslant$5 nm and relative error $\leqslant$15%). Interestingly, the maximum errors coming from lithium, sodium or potassium chlorides, perchlorates or sulfates are substantially lower than the reported maximum relative errors due to the presence of Fe III, which can exceed 80%.[64] Moreover, the interference due to the lithium, sodium or potassium chlorides, perchlorates or sulfates are simpler to correct than Fe III interference due to their negligible influence on the background absorbance, as well as the independence of the quantification error from the TAN concentration, and larger interferent concentration: tens of mM for Fe III[64] against hundreds of mM for the interferents considered in this work. That said, relative errors of up to 25% may not be tolerable in many experiments, necessitating the use of an interference model, such as the one proposed in this work to correct the interference effect. To facilitate understanding of when errors due to the interference from lithium, sodium or potassium chlorides, perchlorates or sulfates become significant, we here calculate the maximum admissible interferent concentration (C_{Int}^{Max}), as defined as the interferent concentration that leads to the maximum admissible measurement error (e_{Max}, in %). The maximum admissible interferent concentration for a given interferent can be estimated using the fitted interference model:

$$C_{Int}^{Max}(e_{Max})$$
$$= \begin{cases} -\dfrac{1}{\alpha_\Gamma} \cdot \ln\left[1 - \dfrac{e_{Max}}{100|\Delta\Gamma|}\right] & \text{if } \Delta\Gamma > \dfrac{e_{Max}}{100} \\ +\infty & otherwise \end{cases} \qquad [6]$$
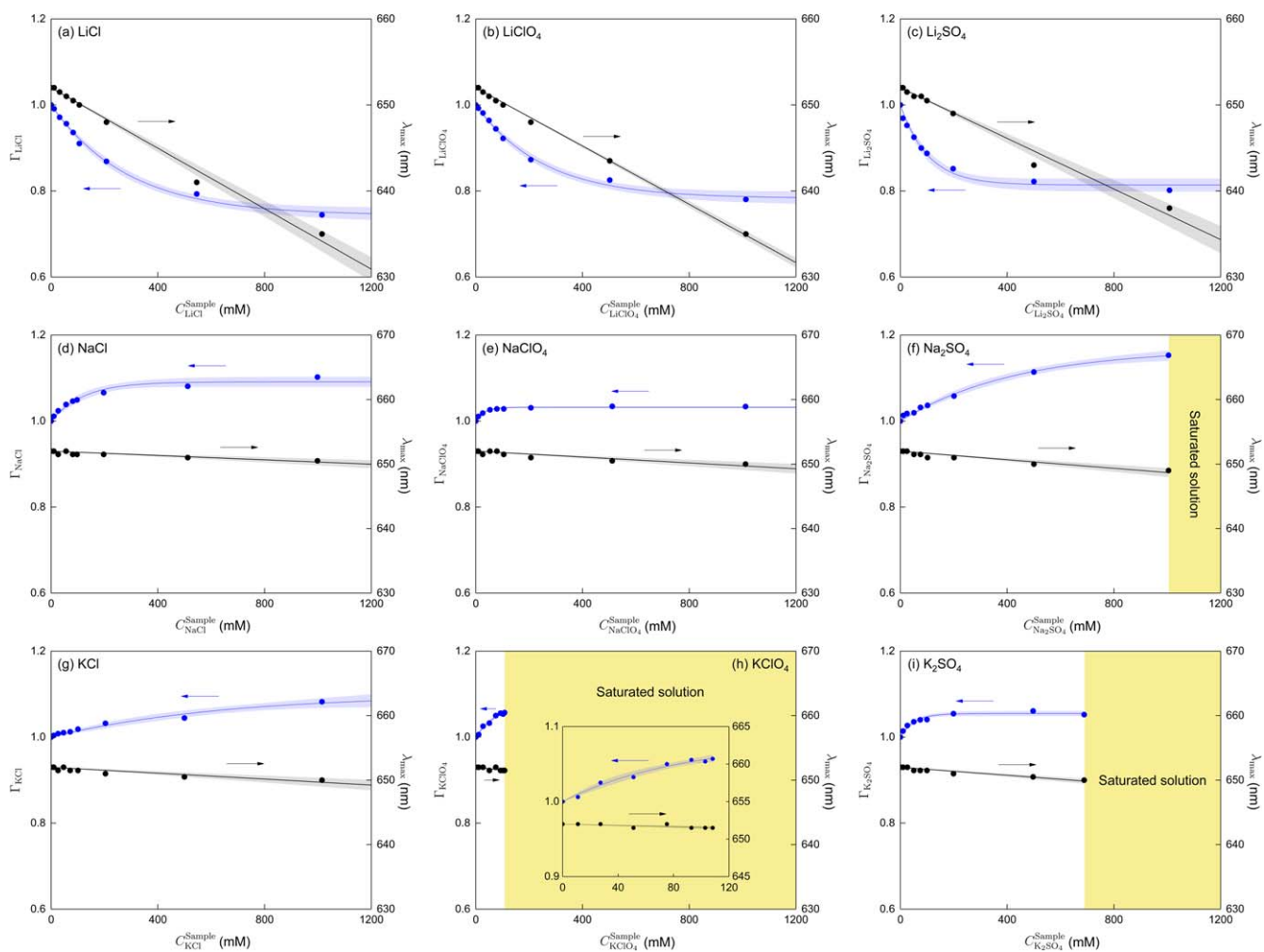
Figure 3. Effect of the interferent concentration on the interference coefficient (Γ, in blue) and the peak position (λ_{max}, in black), for different interferents: (a) LiCl, (b) LiClO$_4$, (c) Li$_2$SO$_4$, (d) NaCl, (e) NaClO$_4$, (f) Na$_2$SO$_4$, (g) KCl, (h) KClO$_4$, (i) K$_2$SO$_4$. The dots correspond to the points calculated from the experimental spectra; the continuous lines corresponds to the fitted empirical models; and the colored (blue and black) regions are the regression 95% confidence bands. The inset in subfigure (h) represents a zoom of the curves. First, the indophenol peak of the experimental spectra from Fig. 2 were fitted to a Gaussian peak (Eq. 3). The fitting was done using a Levenberg-Marquardt algorithm implemented in Labview®, which was initialized with the parameters read directly from the spectrum. On the one hand, the peak position (λ_{max}) was directly obtained from the Gaussian fitting. On the other hand, the interference coefficient (Γ) was calculated from the fitted Gaussian parameters using Eq. 2. Second, the experimental interference coefficient curves (i.e. interference coefficient vs the interferent concentration) were fitted to model (5); whereas, the experimental peak position curves (i.e. peak position vs the interferent concentration) were fitted to model (4). The parameters of the fitted interference model and the fitted peak displacement model, for each one of the interferents, are given in Table I.

where the second case of Eq. 6 corresponds to the case of an interferent whose maximum measurement error is lower or equal to the maximum admissible measurement error. The maximum interferent concentration of the interferents considered in this work was estimated for three different admissible measurement errors: 1%, 5% and 10% (Table II). These values can be used as guidelines to decide whether the interference due to the presence of one of these interferents is significant or not for quantifying ammonia using the salicylate method.

Contributions of the individual cations and anions.—While the cation seems to have a greater effect on the values of the parameter of the peak displacement model (α_λ) and the parameters of the interference model ($\Delta\Gamma$ and α_Γ), the anions also have an appreciable effect on them (Fig. 4). Moreover, the interaction effect between the cation and the anion seems to be moderate, especially in the α_Γ case. Despite the existence of an interaction effect, a superposition linear model (that does not consider the aforementioned interaction) was considered in order to estimate the individual contribution of each

ion to each one of the three model parameters. The superposition model assumes that each one of the three model parameters of a given interferent can be expressed as the sum of the individual contributions of the ions that form that interferent:

$$\vec{x}_{\text{mod}} \equiv \begin{pmatrix} x_{\text{LiCl}} \\ x_{\text{LiClO}_4} \\ x_{\text{Li}_2\text{SO}_4} \\ x_{\text{NaCl}} \\ x_{\text{NaClO}_4} \\ x_{\text{Na}_2\text{SO}_4} \\ x_{\text{KCl}} \\ x_{\text{KClO}_4} \\ x_{\text{K}_2\text{SO}_4} \end{pmatrix} = \boldsymbol{S} \cdot \vec{x}_{\text{ind}} \qquad [7]$$

Where x is one of the three model parameters (α_λ, $\Delta\Gamma$ and α_Γ). $\vec{x}_{\text{mod}}$ is the vector of compound values of parameter x. $\boldsymbol{S}$ and $\vec{x}_{\text{ind}}$ denote the stoichiometry matrix and the vector of individual contributions of each ion, respectively; defined as:
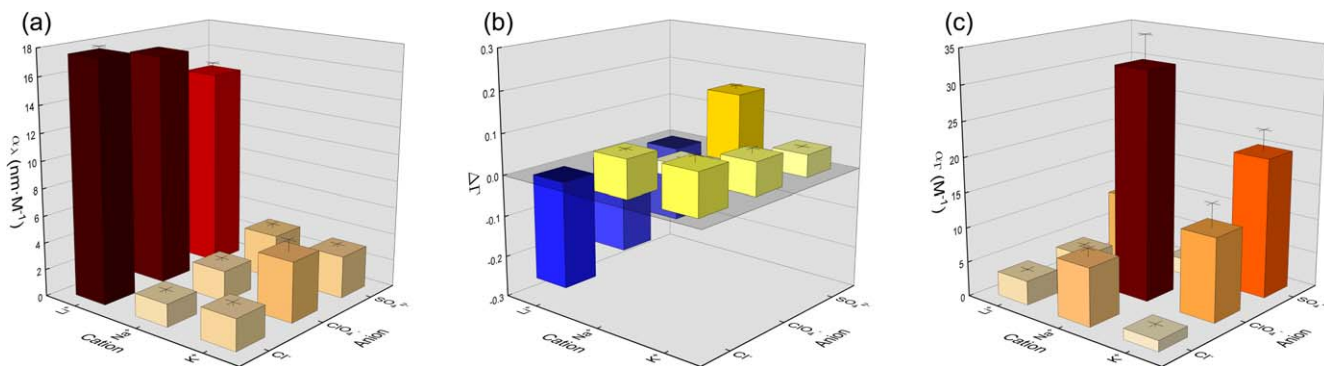
Figure 4. Fitted parameters of the peak displacement model ((a) α_λ) and the interference model ((b) $\Delta\Gamma$; (c) α_Γ) for the different interferents. First, the indophenol peak of the experimental spectra from Fig. 2 were fitted to a Gaussian peak (Eq. 3). The fitting was done using a Levenberg-Marquardt algorithm implemented in Labview®, which was initialized with the parameters read by eye from the spectrum. On the one hand, the peak position (λ_{max}) was directly obtained from the Gaussian fitting. On the other hand, the interference coefficient (Γ) was calculated from the fitted Gaussian parameters using Eq. 2. Second, the experimental interference coefficient curves (i.e. interference coefficient vs the interferent concentration) were fitted to model (5); whereas, the experimental peak position curves (i.e. peak position vs the interferent concentration) were fitted to model (4). The peak displacement model has 1 parameter: α_λ, the peak displacement slope, that corresponds to the peak shift produced by an unitary change in the interferent concentration. The interference model has 2 parameters: $\Delta\Gamma$ and α_Γ. The first one is the maximum change (for very large interferent concentrations) in the interference coefficient. The second one, the absorbance sensibility coefficient, quantifies the sensibility of the interference coefficient to the interferent concentration.

$$S \equiv \begin{pmatrix} 1 & 0 & 0 & 1 & 0 & 0 \\ 1 & 0 & 0 & 0 & 1 & 0 \\ 2 & 0 & 0 & 0 & 0 & 1 \\ 0 & 1 & 0 & 1 & 0 & 0 \\ 0 & 1 & 0 & 0 & 1 & 0 \\ 0 & 2 & 0 & 0 & 0 & 1 \\ 0 & 0 & 1 & 1 & 0 & 0 \\ 0 & 0 & 1 & 0 & 1 & 0 \\ 0 & 0 & 2 & 0 & 0 & 1 \end{pmatrix} \quad [8]$$

$$\vec{x}_{ind} \equiv \begin{pmatrix} x^{Li^+} \\ x^{Na^+} \\ x^{K^+} \\ x^{Cl^-} \\ x^{ClO_4^-} \\ x^{SO_4^{2-}} \end{pmatrix} \quad [9]$$

The fitting of the experimental data to the superposition linear model can be performed solving three optimization problems (one for each model parameter):

$$\min_{\vec{x}_{ind}} \| S \cdot \vec{x}_{ind} - \vec{x}_{exp} \| \quad [10]$$

Where $\vec{x}_{exp}$ denotes the vector of the experimental compound values of parameter x (Table I); and $\| \therefore \|$ represents the conventional $\mathbb{R}^n$ modulus operator. Notably, the superposition linear model captures around 80% of the experimental variation of the peak shift coefficient (Figs. 6a and 6b) and 75% of the experimental variation of the maximum change in the interference coefficient (Figs. 6c and 6d), showing that the effect of a given interferent (of the ones considered in this work) can be mostly explained by the sum of the individual contributions of the constitutive ions. Interestingly, with the exception of Li^+ (which as discussed above seems to influence not only the dye formation reaction, but also alter the formed dye's absorption through coordination), the individual contributions to the peak shift coefficient of the different ions present a moderate correlation with the water-structural contributions to the entropy (S_{str}) of the ions (Table S1[82]) where ions with higher S_{str} have larger individual contributions to the peak shift coefficient. While the set of interferents is too small to generalize this observation (motivating further study), such correlation could suggest that not only can

cation coordination alter the dye's peak absorption wavelength, but this can also be influenced by the water solvation structure around the dye, which can be altered by the presence of ions. Significantly, the superposition linear model only captures around 35% of the experimental variation of the absorbance sensibility coefficient (Figs. 6e and 6f), which shows that the variation of this parameter from interferent to interferent cannot be explained by the superposition principle and that the interaction between the individual interferents plays an important role.

Correcting the interferences on the salicylate method.—Similar to the correction method proposed for Fe III,[64] the interference model proposed in this work can be used to correct the interferences produced by LiCl, LiClO$_4$, Li$_2$SO$_4$, NaCl, NaClO$_4$, Na$_2$SO$_4$, KCl, KClO$_4$ and K$_2$SO$_4$ on the salicylate method. If the concentration of the interferent in the sample is known, the interference model proposed above can be used to calculate the interference coefficient, which can then be used as a correction factor to correct the interference effect. The TAN concentration in the sample can be calculated using the following expression:

$$C_{TAN}^{Sample} = \frac{A_{\lambda_{max}(C_{Int}^{Sample})}(C_{TAN}^{Sample}; C_{Int}^{Sample})}{l \cdot \varepsilon^*_{\lambda_{max}(C_{Int}^{Sample}=0)}(C_{Int}^{Sample}=0) \cdot \Gamma(C_{Int}^{Sample})} \quad [11]$$

Where $\varepsilon^*_{\lambda_{max}(C_{Int}^{Sample}=0)}(C_{Int}^{Sample}=0)$ is obtained from the calibration curve in water samples (Fig. 1a), and $\Gamma(C_{Int}^{Sample})$ is estimated using the interference model (Eq. 5) which requires to first obtain the interference curve (Fig. 2) in order to obtain the experimental interference coefficients and then fit the empirical model. In this case, since there is no background generation unlike in the Fe III case, only these two parameters are required. Once they are known, expression (11) can be used to estimate the TAN concentration in a given sample from its measured maximum absorbance ($A_{\lambda_{max}(C_{Int}^{Sample})}(C_{TAN}^{Sample}; C_{Int}^{Sample})$), correcting in this way the interference effect on the salicylate method.

The great advantage of this method is that it only requires two experimental curves (i.e. the calibration curve in water samples and the interference curve) to correct the interference in a sample with any interferent concentration. In contrast, the experimental correction method (i.e. obtaining the calibration curve in the presence of the corresponding interferent concentration) requires one to obtain a different calibration curve for each sample with a different interferent concentration. Of course, this advantage only makes
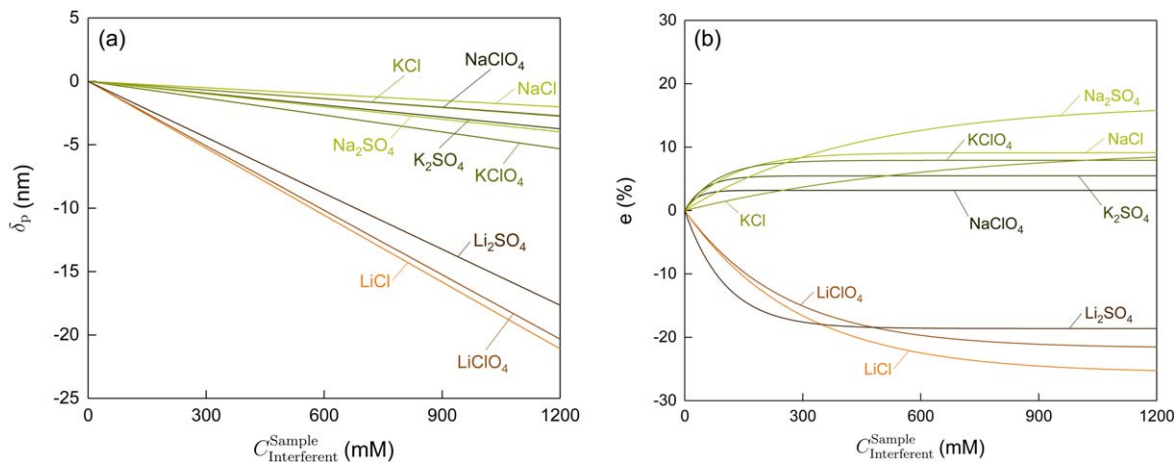
Figure 5. (a) Prediction, using the proposed fitted peak displacement model, of the shift of the indophenol peak (δ_P) as a function of the interferent concentrations in the sample ($C_{Interferent}^{Sample}$), when applying the salicylate method to samples containing different interferents. (b) Prediction, using the proposed fitted interference model, of the relative error (e) in the ammonia quantification using the salicylate method, due to the presence of different interferents in the sample, as a function of the interferent concentrations in the sample. These predictions were made using the fitted peak displacement and interference models for each interferent (Table I).

Table I. Fitted parameters of the peak displacement and interference models. First, the indophenol peak of the experimental spectra from Fig. 2 were fitted to a Gaussian peak (Eq. 3). The fitting was done using a Levenberg-Marquardt algorithm implemented in Labview®, which was initialized with the parameters read by eye from the spectrum. On the one hand, the peak position (λ_{max}) was directly obtained from the Gaussian fitting. On the other hand, the interference coefficient (Γ) was calculated from the fitted Gaussian parameters using Eq. 2. Second, the experimental interference coefficient curves (i.e. interference coefficient vs the interferent concentration) were fitted to model (5); whereas, the experimental peak position curves (i.e. peak position vs the interferent concentration) were fitted to model (4). The peak displacement model has 1 parameter: α_λ, the peak displacement slope, that corresponds to the peak shift produced by an unitary change in the interferent concentration. The interference model has 2 parameters: $\Delta\Gamma$ and α_Γ. The first one is the maximum change (for very large interferent concentrations) in the interference coefficient. The second one, the absorbance sensibility coefficient, quantifies the sensibility of the interference coefficient to the interferent concentration. The fitted parameters are given with their 95% confidence level uncertainties. The determination coefficient (R^2) of each one of the fitted models is also presented, as a quantifier of the goodness of fit.

Interferent	Peak displacement model		Interference model		
	α_λ (nm·M^{-1})	R^2 (%)	$\Delta\Gamma$	α_Γ (M^{-1})	R^2 (%)
LiCl	17.58 ± 0.51	99.02	-0.2567 ± 0.0073	3.47 ± 0.24	99.47
LiClO$_4$	16.94 ± 0.20	99.87	-0.2172 ± 0.0067	3.95 ± 0.30	99.32
Li$_2$SO$_4$	14.71 ± 0.58	98.24	-0.1862 ± 0.0064	9.66 ± 0.91	98.18
NaCl	1.68 ± 0.23	94.48	0.0911 ± 0.0051	8.3 ± 1.2	95.56
NaClO$_4$	2.27 ± 0.27	95.33	0.03194 ± 0.00095	32.5 ± 4.1	97.42
Na$_2$SO$_4$	3.32 ± 0.30	92.80	0.1682 ± 0.0096	2.32 ± 0.28	98.93
KCl	2.30 ± 0.29	96.04	0.099 ± 0.017	1.55 ± 0.47	96.32
KClO$_4$	4.43 ± 0.87	97.85	0.079 ± 0.013	12.0 ± 3.4	98.05
K$_2$SO$_4$	3.12 ± 0.25	93.36	0.0548 ± 0.0026	20.0 ± 3.1	95.06

differences in cases where the interferent concentration changes significantly from sample to sample. When compared to the method proposed for correcting the interferences of Fe III,[64] in this case only two experimental curves are required (instead of the three that are required in the Fe III case), since in the case of the interferents considered in this work, there is no background generation.

Unfortunately, in the case of the interferents considered in this work, the spectrum does not present any secondary feature related to the interferent concentration, unlike in the case of Fe III.[64] Consequently, the interferent concentration cannot be estimated directly from the spectrum itself; which makes impossible to implement autocorrective or semi-autocorrective methods. Therefore, the correction method proposed in this work for LiCl, LiClO$_4$, Li$_2$SO$_4$, NaCl, NaClO$_4$, Na$_2$SO$_4$, KCl, KClO$_4$ and K$_2$SO$_4$ can only be implemented as a non-autocorrective method. Each sample is divided into two aliquots, where the first one is analyzed using the salicylate method while the second one is used to measure the interferent concentration using a suitable quantification method.

The salicylate measurement is then corrected with the interference correction method, using the measured interferent concentration.

The ammonia quantification errors due to the presence of the studied interferents are high enough to be a significant source of uncertainty in NRR experiments in which these interferents are used as electrolytes. The correction method proposed here allows to reduce these uncertainties. As the correction method only reduces errors, but does not eliminate them, colorimetric ammonia quantification (even if corrected) should be reserved to the initial screening experiments, which results should always be verified using techniques less prone to interferences, such as ^{15}N isotope labelling.

Conclusions

In this work, the interference due to the presence of LiCl, LiClO$_4$, Li$_2$SO$_4$, NaCl, NaClO$_4$, Na$_2$SO$_4$, KCl, KClO$_4$, and K$_2$SO$_4$ salts on the salicylate method was systematically studied and interference and peak shift models were proposed. All of the nine considered

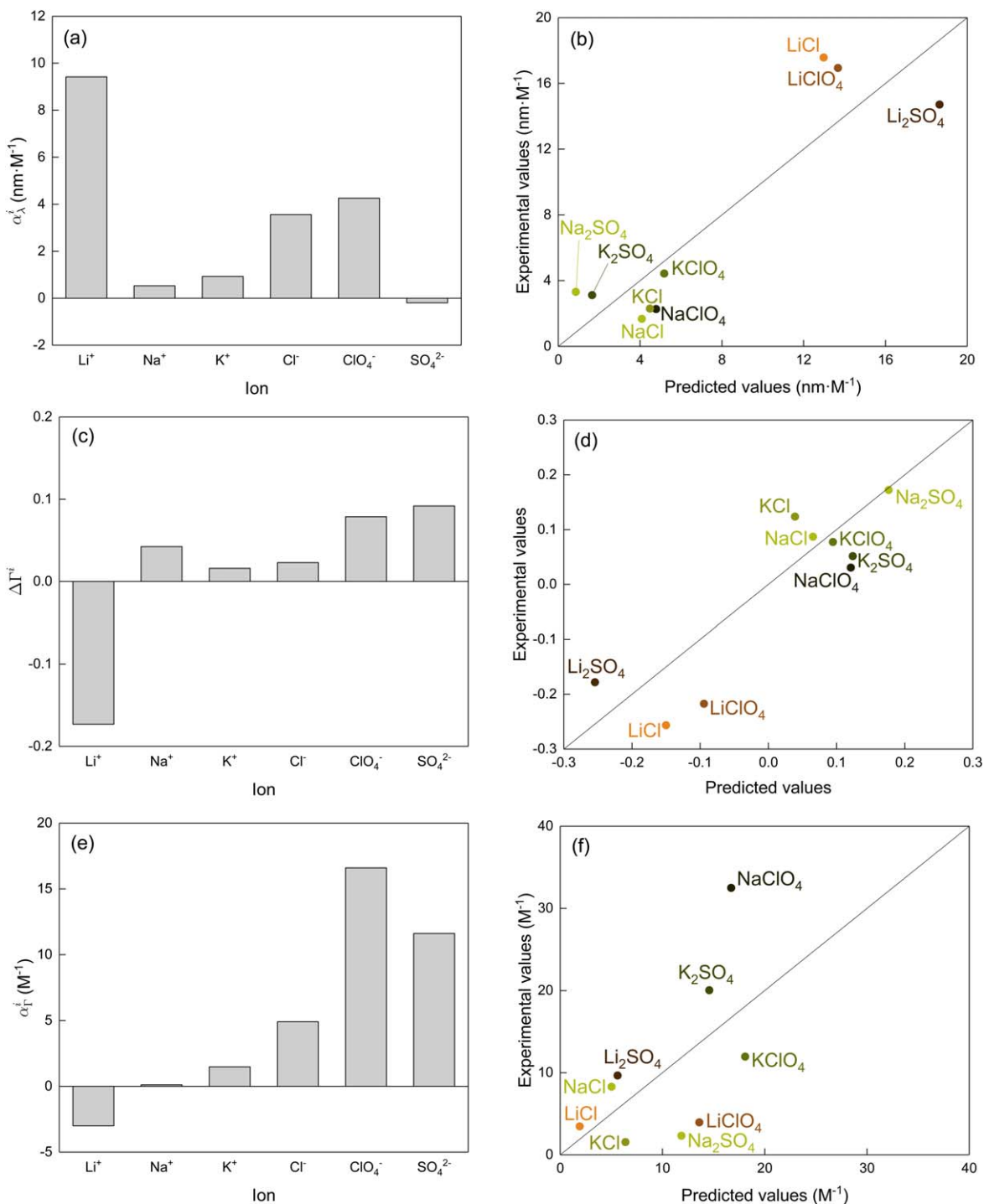**Figure 6.** Fitted non-interaction model for (a) (b) the peak displacement slope (α_λ), (c) (d) the maximum change in the interference coefficient ($\Delta\Gamma$), and (e) (f) the absorbance sensibility coefficient (α_Γ). (a) (c) (e) Fitted individual contribution of each ion to the corresponding parameter. (b) (d) (f) Predicted vs experimental plot of the fitted non-interaction model for that parameter. The non-interaction models (Eq. 7) were fitted by solving the optimization problem (10) using a genetic algorithm implemented in Labview®. The determination coefficients (R^2) of the fitted models are: 80.66% for α_λ, 73.94% for $\Delta\Gamma$, and 32.71% for α_Γ.

interferents were found to cause a hypsochromic shift (i.e. blue shift) in the dye spectrum obtained with the salicylate method where TD-DFT calculations suggest that this hypsochromic shift stems from cation coordination with the indophenol dye. Li-containing interferents were observed to cause a strong negative interference on the ammonia quantification peak of the salicylate method, whereas Na- and K-containing interferents resulted in a slight to moderate positive interference on the ammonia quantification peak. Such

salt-dependent changes in molar absorbance of the indophenol dye were attributed to changes in the stereochemistry, which was supported by TD-DFT calculations. Significantly, the presence of lithium, sodium and potassium chlorides, perchlorates and sulfates in the sample was found to lead to relative errors in ammonia quantification up to 25%, motivating the development of an interference model to allow for corrections of errors due to these interferents. Based on their maximum admissible concentration in

Table II. Maximum admissible concentration in the sample for different interferents, for different maximum admissible measurement errors (1%, 5% and 10%) in the ammonia quantification using the salicylate method. If a sample with an interfernt concentration larger than the reported value is analyzed using the salicylate method, the measurement error in the ammonia quantification will be larger than the maximum admissible measurement error. These maximum concentrations were calculated using the fitted interference model for each interferent (Table I) in Eq. 6.

Interferent	C_{Int}^{max} (1%) (mM)	C_{Int}^{max} (5%) (mM)	C_{Int}^{max} (10%) (mM)
LiCl	11.8	64.3	146.5
LiClO$_4$	11.9	66.0	155.6
Li$_2$SO$_4$	6.7	38.4	96.1
NaCl	17.2	120.5	$+\infty$
NaClO$_4$	13.1	$+\infty$	$+\infty$
Na$_2$SO$_4$	31.0	177.6	449.9
KCl	89.3	548.5	1749.1
KClO$_4$	10.5	79.0	$+\infty$
K$_2$SO$_4$	12.3	199.2	$+\infty$

the sample for a 1% maximum admissible measurement error in the ammonia quantification, the tested interferents can be ranked from stronger interferent (i.e. lower admissible concentration) to weaker interferent: Li$_2$SO$_4$, KClO$_4$, LiCl, LiClO$_4$, K$_2$SO$_4$, NaClO$_4$, NaCl, Na$_2$SO$_4$, KCl. The correction method requires obtaining two experimental curves: the calibration curve in water samples and the interference curve, which can save significant experimental effort if the interferent concentration changes significantly between samples. Unfortunately, the correction method proposed in this work can only be implemented as a non-autocorrective method where each sample is divided into two aliquots, one analyzed with the salicylate method, and the other one using a suitable interferent quantification method. The model developed in this work enables significantly increased accuracy of the salicylate method for NRR experiments with supporting electrolyte, which is vital to ensure rigorous and reproducible findings.

ORCID

Juan José Giner-Sanz https://orcid.org/0000-0003-0441-6102
Graham M. Leverick https://orcid.org/0000-0001-8541-4381
Yang Shao-Horn https://orcid.org/0000-0001-8714-2121

References

1. J. Erisman, A. Bleeker, J. Galloway, and M. S. Sutton, *Environ. Pollut.*, **150**, 140 (2007).
2. T. Cottrell, "The strengths of chemical bonds." *Butterworths Scientific* (Publications, London) (1958).
3. H. Jia and E. Quadrelli, *Chem. Soc. Rev.*, **43**, 547 (2014).
4. J. Guo and P. Chen, *Accounts Chem. Res.*, **54**, 2434 (2021).
5. J. Erisman, M. Sutton, J. Galloway, Z. Klimont, and W. Winiwarter, *Nat. Geosci.*, **1**, 636 (2008).
6. USGS National Minerals Information Center, Nitrogen statistics and information (2020), https://usgs.gov/centers/national-minerals-information-center/nitrogen-statistics-and-information.
7. L. Wang, M. Xia, H. Wang, K. Huang, C. Qian, C. Maravelias, and G. Ozin, *Joule*, **2**, 1055 (2018).
8. L. Apodaca, *Nitrogen (fixed) - Ammonia* (2021).
9. J. Lim, C. Fernández, S. Lee, and M. Hatzell, *ACS Energy Lett.*, **6**, 3676 (2021).
10. V. Smil, *Nature*, **400**, 415 (1999).
11. I. H. S. Markit, *Ammonia in Chemical Economics Handbook* (S & P Global) (2020), Ammonia in Chemical Economics Handbook.
12. R. Schögl, 'Carbons' in *Handbook of heterogeneous catalysis* (Wiley, New York) (2008).
13. S. Feng, W. Gao, Q. Wang, Y. Guan, H. Yan, H. Wu, H. Cao, J. Guo, and P. Chen, *J. Mater. Chem. A*, **9**, 1039 (2021).
14. Q. Wang, J. Guo, and P. Chen, *Joule*, **4**, 705 (2020).
15. A. Klerke, C. Christensen, J. Nørskov, and T. Vegge, *J. Mater. Chem.*, **18**, 2304 (2008).
16. C. Smith, A. Hill, and L. Torrente-Murciano, *Energ. Environ. Sci.*, **13**, 331 (2020).
17. Y. Liu, C. Fernández, S. Varanasi, N. Bui, L. Song, and M. Hatzell, *ACS Energy Lett.*, **7**, 24 (2021).
18. P. Wang, F. Chang, W. Gao, J. Guo, G. Wu, T. He, and P. Chen, *Nat. Chem.*, **9**, 64 (2017).
19. C. Van der Ham, M. Koper, and D. Hetterscheid, *Chem. Soc. Rev.*, **43**, 5183 (2014).
20. Q. Wang, J. Guo, and P. Chen, *J. Energy Chem.*, **36**, 25 (2019).
21. A. Tricker, K. Hebisch, M. Buchmann, Y. Liu, M. Rose, E. Stavitski, A. Medford, M. Hatzell, and C. Sievers, *ACS Energy Lett.*, **5**, 3362 (2020).
22. C. Fernandez and M. Hatzell, *J. Electrochem. Soc.*, **167**, 143504 (2020).
23. V. Kyriakou, I. Garagounis, A. Vourros, E. Vasileiou, and M. Stoukides, *Joule*, **4**, 142 (2020).
24. F. Chang, W. Gao, J. Guo, and P. Chen, *Adv. Mater.*, **33**, 2005721 (2021).
25. B. Suryanto, H. Du, D. Wang, J. Chen, A. Simonov, and D. MacFarlane, *Nat. Catal.*, **2**, 290 (2019).
26. D. MacFarlane, P. Cherepanov, J. Choi, B. Suryanto, R. Hodgetts, J. Bakker, F. Vallana, and A. Simonov, *Joule*, **4**, 1186 (2000).
27. H. Iriawan, S. Andersen, X. Zhang, B. Comer, J. Barrio, P. Chen, A. Medford, I. Stephens, I. Chorkendorff, and Y. Shao-Horn, *Nat. Rev. Methods Primers*, **1**, 1 (2021).
28. M. Hattori, S. Iijima, T. Nakao, H. Hosono, and M. Hara, *Nat. Commun.*, **11**, 1 (2020).
29. S. Wu, Y. Peng, T. Chen, J. Mo, A. Large, I. McPherson, I. Chou, I. Wilkinson, F. Venturini, and D. Grinter, *ACS Catal.*, **10**, 5614 (2020).
30. T. Ye, S. Park, Y. Lu, J. Li, M. Sasase, M. Kitano, T. Tada, and H. Hosono, *Nature*, **583**, 391 (2020).
31. A. Tsuneto, A. Kudo, and T. Sakata, *J. Electroanal. Chem.*, **367**, 183 (1994).
32. Y. Hao, Y. Guo, L. Chen, M. Shu, X. Wang, T. Bu, W. Gao, N. Zhang, X. Su, and X. Feng, *Nat. Catal.*, **2**, 448 (2019).
33. S. Andersen, M. Statt, V. Bukas, S. Shapel, J. Pedersen, K. Krempl, M. Saccoccio, D. Chakraborty, J. Kibsgaard, and P. Vesborg, *Energ. Environ. Sci.*, **13**, 4291 (2020).
34. Y. Wang et al., *Angew. Chem. Int. Edit.*, **58**, 9464 (2019).
35. N. Zhang, A. Jalil, D. Wu, S. Chen, Y. Liu, C. Gao, W. Ye, Z. Qi, H. Ju, and C. Wang, *J. Am. Chem. Soc.*, **140**, 9434 (2018).
36. S. Wang, X. Hai, X. Ding, K. Chang, Y. Xiang, X. Meng, Z. Yang, H. Chen, and J. Ye, *Adv. Mater.*, **29**, 1701774 (2017).
37. D. Zhu, L. Zhang, R. Ruther, and R. Hamers, *Nat. Mater.*, **12**, 836 (2013).
38. Y. Jang, A. Lindberg, M. Lumley, and K. Choi, *ACS Energy Lett.*, **5**, 1834 (2020).
39. M. Ali, F. Zhou, K. Chen, C. Kotzur, C. Xiao, L. Bourgeois, X. Zhang, and D. MacFarlane, *Nat. Commun.*, **7**, 1 (2016).
40. M. Vu, C. Nguyen, and T. Do, *ACS Sustain. Chem. Eng.*, **8**, 12321 (2020).
41. L. Winter and J. Chen, *Joule*, **5**, 300 (2021).
42. L. Winter, B. Ashford, J. Hong, A. Murphy, and J. Chen, *ACS Catal.*, **10**, 14763 (2020).
43. S. Reichle, M. Felderhoff, and F. Schüth, *Angew. Chem. Int. Edit.*, **60**, 26389 (2021).
44. L. Shi, Y. Yin, S. Wang, X. Xu, H. Wu, J. Zhang, S. Wang, and H. Sun, *Appl. Catal. B: Environ.*, **278**, 119325 (2020).
45. D. Li, X. Xu, Z. Li, T. Wang, and C. Wang, *Trend. Anal. Chem.*, **127**, 115890 (2020).
46. C. Wang, Z. Li, Z. Pan, and D. Li, *Comput. Electron. Agr.*, **150**, 364 (2018).
47. F. Koch and T. McMeekin, *J. Am. Chem. Soc.*, **46**, 2066 (1924).
48. I. Ivancič and D. Degobbis, *Water Res.*, **18**, 1143 (1984).
49. A. LeDuy and R. Samson, *Biotechnol. Lett.*, **4**, 303 (1982).
50. C. Wang, T. Wang, Z. Li, X. Xu, X. Zhang, and D. Li, *Biosensors*, **11**, 335 (2021).
51. M. Rey, *J. Chromatogr. A*, **920**, 61 (2001).
52. G. Duan, Y. Ren, Y. Tang, Y. Sun, Y. Chen, P. Wan, and X. Yang, *ChemSusChem*, **13**, 88 (2020).
53. J. McEnaney, A. Singh, J. Schwalbe, J. Kibsgaard, J. Lin, M. Cargnello, T. Jaramillo, and J. K. Nørskov, *Energ. Environ. Sci.*, **10**, 1621 (2017).
54. J. Liu, M. Kelley, W. Wu, A. Banerjee, A. Douvalis, J. Wu, Y. Zhang, G. Schatz, and M. Kanatzidis, *P. Natl. A. Sci.*, **113**, 5530 (2016).
55. S. Andersen et al., *Nature*, **570**, 504 (2019).
56. J. Choi, B. Suryanto, D. Wang, H. Du, R. Hodgetts, F. Vallana, D. MacFarlane, and A. Simonov, *Nat. Commun.*, **1**, 1 (2020).
57. Y. Song et al., *Sci. Adv.*, **4**, 1700336 (2018).

58. A. Cerda, M. Oms, R. Forteza, and V. Cerda, *Anal. Chim. Acta*, **311**, 165 (1995).
59. C. Molins-Legua, S. Meseguer-Lloret, Y. Moliner-Martinez, and P. Campíns-Falcó, *Trend. Anal. Chem.*, **25**, 282 (2006).
60. A. Kempers and C. Kok, *Anal. Chim. Acta*, **221**, 147 (1989).
61. P. Searle, *Analyst*, **109**, 549 (1984).
62. R. Willis, M. Montgomery, and P. Allen, *J. Agr. Food Chem.*, **44**, 1804 (1996).
63. F. Jüttner, *Fresenius' J. Anal. Chem.*, **363**, 128 (1999).
64. J. J. Giner-Sanz, G. Leverick, V. Perez-Herranz, and Y. Shao-Horn, *J. Electrochem. Soc.*, **167**, 134519 (2020).
65. H. Boo and T. Ma, *Microchim. Acta*, **66**, 515 (1976).
66. Y. Zhang, J. Hu, C. Zhang, Y. Liu, M. Xu, Y. Xue, L. Liu, and M. Leung, *J. Mater. Chem. A*, **8**, 9091 (2020).
67. Q. Liu, X. Zhang, J. Wang, Y. Zhang, S. Bian, Z. Cheng, N. Kang, H. Huang, S. Gu, and Y. Wang, *Angew. Chem. Int. Edit.*, **59**, 14383 (2020).
68. R. Hao, W. Sun, Q. Liu, X. Liu, J. Chen, X. Lv, W. Li, Y. Liu, and Z. Shen, *Small*, **16**, 2000015 (2020).
69. H. Cheng, P. Cui, F. Wang, L. Ding, and H. Wang, *Angew. Chem.*, **131**, 15687 (2019).
70. L. Pospíšil, M. Hromadová, M. Gál, J. Bulíčková, R. Sokolová, and N. Fanelli, *Electrochim. Acta*, **53**, 7445 (2008).
71. L. Zhang, M. Cong, X. Ding, Y. Jin, F. Xu, Y. Wang, L. Chen, and L. Zhang, *Angew. Chem.*, **132**, 10980 (2020).
72. C. Bower, T. Holm-Hansen, and J. Can., *Fish. Aquat. Sci.*, **37**, 794 (1980).
73. P. Le and C. Boyd, *J. World Aquacult. Soc.*, **43**, 885 (2012).
74. J. J. Giner-Sanz, G. Leverick, V. Pérez-Herranz, and Y. Shao-Horn, *J. Electroanal. Chem.*, **896**, 115250 (2021).
75. J. Tomasi, B. Mennucci, and R. Cammi, *R. Chem. Rev.*, **105**, 2999 (2005).
76. M. Cossi and V. Barone, *J. Chem. Phys.*, **115**, 47084717 (2001).
77. D. Jacquemin, E. Perpète, G. Scuseria, I. Ciofini, and C. Adamo, *J. Chem. Theory Comput.*, **4**, 123 (2008).
78. M. Ernzerhof and G. Scuseria, *J. Chem. Phys.*, **110**, 5029 (1999).
79. C. Adamo and V. Barone, *J. Chem. Phys.*, **110**, 61586170 (1999).
80. M. Frisch et al., *Gaussian 16 Revision C.01* (Gaussian Inc, Wallingford CT) (2016).
81. D. Jacquemin, E. Perpète, G. Scuseria, I. Ciofini, and C. Adamo, *Chem. Phys. Lett.*, **465**, 226 (2008).
82. Y. Marcus, *J. Solution Chem.*, **23**, 831 (1994).